SOLID-STATE PHYSICS

Interface-induced superconductivity in magnetic topological insulators

Hemian Yi[1]†, Yi-Fan Zhao[1]†, Ying-Ting Chan[2]†, Jiaqi Cai[3]†, Ruobing Mei[1], Xianxin Wu[4], Zi-Jie Yan[1], Ling-Jie Zhou[1], Ruoxi Zhang[1], Zihao Wang[1], Stephen Paolini[1], Run Xiao[1], Ke Wang[5], Anthony R. Richardella[1,5], John Singleton[6], Laurel E. Winter[6], Thomas Prokscha[7], Zaher Salman[7], Andreas Suter[7], Purnima P. Balakrishnan[8], Alexander J. Grutter[8], Moses H. W. Chan[1], Nitin Samarth[1,5,9], Xiaodong Xu[3,10], Weida Wu[2]*, Chao-Xing Liu[1]*, Cui-Zu Chang[1,5]*

The interface between two different materials can show unexpected quantum phenomena. In this study, we used molecular beam epitaxy to synthesize heterostructures formed by stacking together two magnetic materials, a ferromagnetic topological insulator (TI) and an antiferromagnetic iron chalcogenide (FeTe). We observed emergent interface-induced superconductivity in these heterostructures and demonstrated the co-occurrence of superconductivity, ferromagnetism, and topological band structure in the magnetic TI layer—the three essential ingredients of chiral topological superconductivity (TSC). The unusual coexistence of ferromagnetism and superconductivity is accompanied by a high upper critical magnetic field that exceeds the Pauli paramagnetic limit for conventional superconductors at low temperatures. These magnetic TI/FeTe heterostructures with robust superconductivity and atomically sharp interfaces provide an ideal wafer-scale platform for the exploration of chiral TSC and Majorana physics.

Superconductivity is a macroscopic quantum phenomenon in which electrons travel without resistance. The vanishing resistivity is caused by the spontaneous condensation of bosonic Cooper pairs (*1*, *2*). Aside from natural compounds, superconductivity also emerges in artificially constructed heterostructures such as $LaAlO_3$/$SrTiO_3$ (*3*, *4*) and $La_{1.55}Sr_{0.45}CuO_4$/La_2CuO_4 (*5*), wherein the parent materials themselves are not superconductors. Moreover, an unusual form of superconductivity known as topological superconductivity (TSC) has been proposed to emerge in heterostructures formed by a material with strong spin-orbit coupling (SOC) and s-wave superconductivity (*6*–*8*). Over the past decade, the potential of realizing TSC in such heterostructures has attracted much attention, driven by the possibility that the excitations of a topological superconductor [i.e., Majorana zero modes (MZMs)] can be used for fault-tolerant topological quantum computation (*9*, *10*).

Topological insulators (TIs) are materials with extremely strong SOC, in which the interior is insulating but electrons can travel freely along the edges and surfaces (*11*, *12*). These qualities make TIs a natural platform to use in engineering TSC (*13*). However, trapping MZMs in a TI/superconductor heterostructure requires the external breaking of time-reversal symmetry. This requirement often inherently suppresses superconductivity and destroys the TSC phase. Magnetic TI/superconductor heterostructures offer an alternative platform for creating the (chiral) TSC phase and MZMs at zero magnetic field. This scheme exploits the quantum anomalous Hall (QAH) effect to realize chiral Majorana modes propagating along the one-dimensional (1D) boundaries of the sample (*14*–*16*). This approach allows for constructing Majorana interferometry that provides both a probe of coherent Majorana physics and allows for the readout of topological qubits (*17*, *18*). The realization of the QAH effect in molecular beam epitaxy (MBE)–grown magnetic TI, specifically Cr- and/or V-doped $(Bi,Sb)_2Te_3$ films or heterostructures (*19*), now provides a well-controlled material basis for designing a TSC platform derived from magnetic TI/superconductor heterostructures.

To date, QAH/superconductor hybrid structures have been fabricated by sputtering a thick s-wave superconductor (e.g., ~100-nm Nb) layer on magnetic TI films (*16*). These superconducting films are usually polycrystalline, which weakens their proximity effect across the QAH/superconductor interface (*16*). QAH/superconductor heterostructures with atomically sharp interfaces are highly desirable for the exploration of chiral TSC. However, in practice, the superconductivity in MBE-grown thin films is usually suppressed or disappears once a magnetic layer is grown on top, primarily owing to the effective pair-breaking mechanism of spin-flip scattering at the interface (*20*). As an alternative, QAH/nonsuperconducting material heterostructures with interfacial superconductivity that host chiral TSC are being pursued. This arrangement fulfills the three essential ingredients of chiral TSC: superconducting, ferromagnetic, and topological orders (*14*). Recently, superconductivity has been found in Bi_2Te_3/FeTe and Sb_2Te_3/FeTe heterostructures with zero-resistance superconducting temperatures $T_{c,0}$ of ~11.5 and ~3.1 K, respectively (*21*, *22*). $(Bi/Sb)_2Te_3$ is a prototype 3D TI (*23*–*25*), whereas FeTe is a nonsuperconducting antiferromagnetic iron chalcogenide (*26*–*28*). Moreover, because $(Bi/Sb)_2Te_3$ with and without Cr doping share the same lattice structure and similar growth recipes, there is an opportunity to synthesize the Cr-doped $(Bi,Sb)_2Te_3$ films (*19*) on an antiferromagnetic FeTe layer to form Cr-doped $(Bi,Sb)_2Te_3$/FeTe heterostructures (Fig. 1A).

In this work, we used MBE to fabricate heterostructures formed by m quintuple layer (QL) ferromagnetic TI Cr-doped $(Bi,Sb)_2Te_3$ and n unit cell (UC) antiferromagnetic iron chalcogenide FeTe films. Below we denote mQL Cr-doped $(Bi/Sb)_2Te_3$/nUC FeTe as the (m,n) heterostructure. We find that these Cr-doped $(Bi/Sb)_2Te_3$/FeTe heterostructures have an atomically sharp interface. By performing electrical transport, reflective magnetic circular dichroism (RMCD), magnetic force microscopy (MFM), scanning tunneling microscopy and spectroscopy (STM/S), low energy muon spin relaxation (LE-μSR), and angle-resolved photoemission spectroscopy (ARPES) measurements (*29*), we reveal and characterize emergent interface-induced superconductivity in Cr-doped $(Bi,Sb)_2Te_3$/FeTe heterostructures and demonstrate the co-occurrence of superconductivity, ferromagnetism, and topological order in the Cr-doped $(Bi,Sb)_2Te_3$ layer. We also find the upper critical magnetic field of the emergent superconductivity to be very high (>40 T), which may be responsible for the robust superconductivity in an entirely magnetic heterostructure that interfaces a ferromagnet with an antiferromagnet.

Interface-induced superconductivity in magnetic TI/FeTe heterostructures

We first characterized the Cr-doped $(Bi,Sb)_2Te_3$/FeTe heterostructures. Despite the different lattice structures (hexagonal versus cubic), both layers show sharp and streaky "1×1" reflection high-energy electron diffraction patterns (fig. S1), presumably owing to the hybrid symmetry epitaxy (*30*). X-ray diffraction (XRD) spectra show peaks of both layers, further confirming

[1]Department of Physics, The Pennsylvania State University, University Park, PA 16802, USA. [2]Department of Physics and Astronomy, Rutgers University, Piscataway, NJ 08854, USA. [3]Department of Physics, University of Washington, Seattle, WA 98195, USA. [4]CAS Key Laboratory of Theoretical Physics, Institute of Theoretical Physics, Chinese Academy of Sciences, Beijing 100190, China. [5]Materials Research Institute, The Pennsylvania State University, University Park, PA 16802, USA. [6]National High Magnetic Field Laboratory, Los Alamos, NM 87544, USA. [7]Laboratory for Muon Spectroscopy, Paul Scherrer Institute, 5232 Villigen PSI, Switzerland. [8]NIST Center for Neutron Research, National Institute of Standards and Technology, Gaithersburg, MD 20899, USA. [9]Department of Materials Science and Engineering, The Pennsylvania State University, University Park, PA 16802, USA. [10]Department of Materials Science and Engineering, University of Washington, Seattle, WA 98195, USA.
*Corresponding author. Email: wdwu@physics.rutgers.edu (W.W.); cxl56@psu.edu (C.-X.L.); cxc955@psu.edu (C.-Z.C.)
†These authors contributed equally to this work.

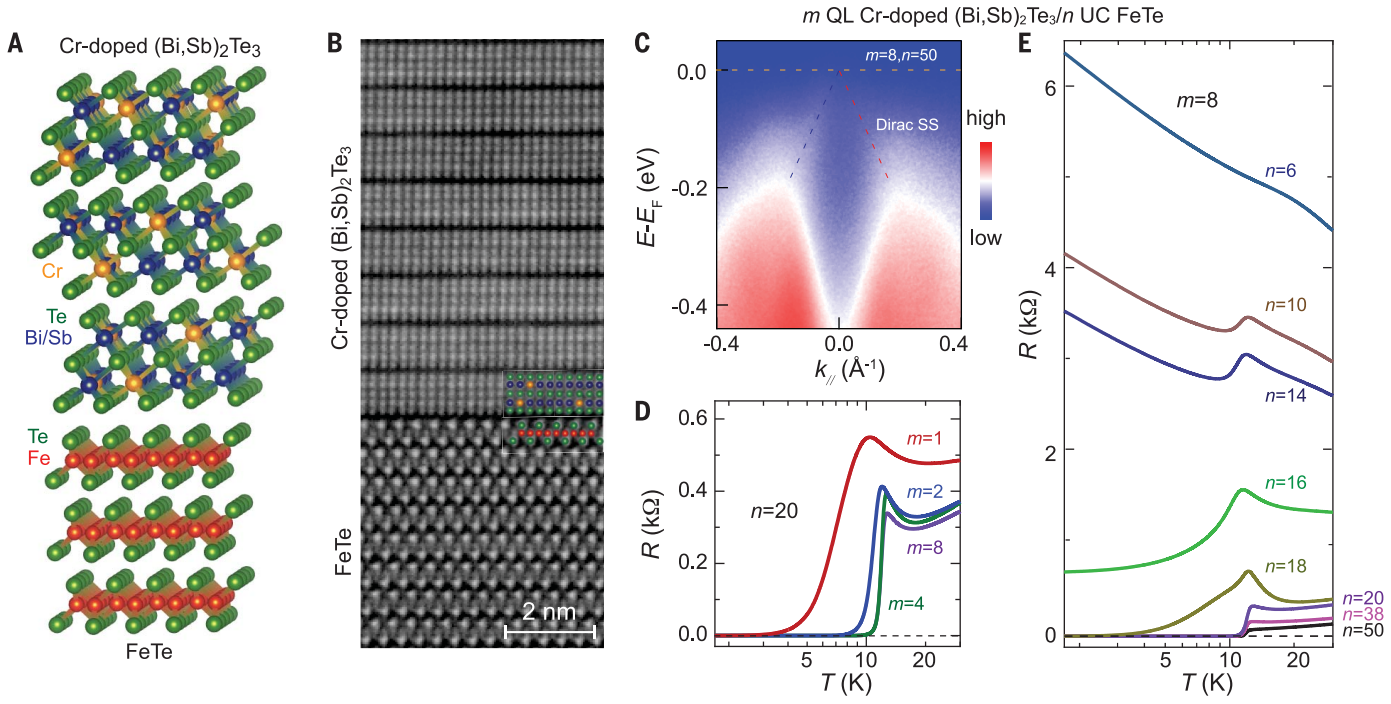

Fig. 1. Interface-induced superconductivity in Cr-doped $(Bi,Sb)_2Te_3$/FeTe heterostructures. (**A**) Schematic lattice structure of the Cr-doped $(Bi,Sb)_2Te_3$/FeTe heterostructure. (**B**) Cross-sectional STEM image of the (8,50) heterostructures grown on heat-treated $SrTiO_3$(100) substrate. (**C**) In situ ARPES band map of the (8,50) heterostructure. The Dirac point is located near the chemical potential. The ARPES measurements were performed at room temperature. (**D**) Temperature dependence of the sheet longitudinal resistance R of the (m,20) heterostructures with m = 1, 2, 4, and 8. (**E**) Temperature dependence of R of the (8,n) heterostructures with $6 \leq n \leq 50$.

the high crystalline property of the Cr-doped $(Bi,Sb)_2Te_3$/FeTe heterostructures (fig. S2). Cross-sectional scanning transmission electron microscopy (STEM) measurements reveal an atomically sharp interface across Cr-doped $(Bi,Sb)_2Te_3$ and FeTe (Fig. 1B and fig. S3). The QL structure of the Cr-doped $(Bi,Sb)_2Te_3$ layer and the trilayer structure of the FeTe layer are seen. To examine the topological band structure, we performed in vacuo ARPES measurements on an (8,50) heterostructure (Fig. 1C). Linearly dispersing Dirac surface states crossing the chemical potential are observed, consistent with the band spectra of the QAH samples at room temperature (*19*, *31*). Indeed, we observe a well-quantized QAH effect in an 8QL Cr-doped $(Bi,Sb)_2Te_3$ layer on $SrTiO_3$(111) substrates (fig. S4).

Next, we performed ex situ transport measurements on a series of Cr-doped $(Bi,Sb)_2Te_3$/FeTe heterostructures. Figure 1D shows the temperature dependence of the sheet longitudinal resistance (i.e., R-T curves) of (m,20) heterostructures. Although the 20UC FeTe film grown on $SrTiO_3$(100) shows nonsuperconducting antiferromagnetic behavior (fig. S5), superconductivity appears after the deposition of 1QL Cr-doped $(Bi,Sb)_2Te_3$ layer, showing clear evidence of interface-triggered superconductivity. For the m = 1 sample, the onset $T_{c,onset}$ and the zero-resistance $T_{c,0}$ are ~9.6 and ~2.9 K, respectively. With increasing m, $T_{c,onset}$ increases slightly, but $T_{c,0}$ increases much more before showing saturation for $m \geq 4$. For the m = 8 sample, $T_{c,onset}$ and $T_{c,0}$ appear to show optimal values of ~12.4 and ~10.0 K, respectively (Fig. 1D).

We therefore stayed with m = 8 and systematically studied the evolution of the emergent superconductivity as a function of the number of FeTe layers, n (Fig. 1E). We find that the $n \geq 20$ samples show sharp superconducting transitions with $T_{c,0}$ ranging between 10.0 and 11.4 K. When n is reduced from 20, the superconductivity is suppressed and the superconducting transition window broadens, indicating enhanced phase fluctuations possibly resulting from the spatial confinement of the Cooper pairs (*32*). For the n =18 sample, $T_{c,onset}$ ~ 12.2 K and $T_{c,0}$ ~ 2.0 K (Fig. 1E). For the $n \leq 16$ samples, the zero-resistance state fades away, but the hump feature near $T_{c,onset}$ persists, indicating the formation of local superconducting order without long-range phase coherence. For $T < T_{c,onset}$, the n = 16 sample shows metallic behavior, whereas for the $n \leq 14$ samples, R first drops and then increases to a few kilohms (Fig. 1E). The upturn feature in $n \leq 14$ samples indicates the presence of an insulating phase in the low-temperature regime. We note that the observed superconductor-metal-insulator phase transition for $n \leq 16$ is analogous to that found in patterned cuprate superconductors, in which the nearly linear R-T curve before entering the zero-resistance state has been attributed to the disorder-induced Bosonic anomalous metal phase (*33*).

Coexistence of ferromagnetism and superconductivity

To confirm the existence of ferromagnetism, we first performed electrical transport measurements on the Cr-doped $(Bi,Sb)_2Te_3$/FeTe heterostructures. Figure 2A shows the R-T curve of the (8,50) heterostructure from room temperature down to T = 2 K. Its $T_{c,onset}$ is ~12.4 K and $T_{c,0}$ is ~11.4 K. Notably, we observe a broad semiconducting-to-metallic crossover near T ~ 60 K. Such behavior in the R-T curve of FeTe has been associated with the paramagnetic-to-antiferromagnetic phase transition (fig. S5) (*22*). Figure 2B shows the Hall traces near the superconducting transition regime. At T = 10 K, which is below $T_{c,0}$ ~ 11.4 K, the Hall resistance R_{yx} value is zero. The vanishing value of R_{yx} here is a result of the zero-resistance state of the superconducting phase. At T = 12 K, which is located in the superconducting transition regime (i.e.,

$T_{c,0} < T < T_{c,onset}$), a small hysteresis loop appears, implying the existence of ferromagnetism. By further increasing T to 14 K, the sample shows a hysteresis loop with larger R_{yx}, further confirming the existence of the ferromagnetism in Cr-doped $(Bi,Sb)_2Te_3$/FeTe heterostructure above its superconducting $T_{c,onset}$ (Fig. 2B).

To demonstrate the coexistence of superconductivity and ferromagnetism at $T < T_{c,0}$, we performed RMCD measurements on the same (8,50) heterostructure. Figure 2C shows the magnetic field $\mu_0 H$ dependence of the RMCD signal at 2 K ≤ T ≤ 14 K. Hysteresis loops are observed in the entire temperature range, demonstrating the persistence of ferromagnetism in the superconducting regime. For $T > T_{c,0}$, the observed hysteresis loops and coercive field $\mu_0 H_c$ agree well with the value deduced from the Hall measurements at the same temperature (Fig. 2, B and C). Similar behavior is observed in the (8,20) heterostructure (fig. S6).

The coexistence of superconductivity and ferromagnetism is further supported by direct visualization of ferromagnetic domains using MFM with in situ transport measurements. Figure 3, A to H, shows the MFM images of magnetic domains in the (8,20) heterostructure at different $\mu_0 H$ and T = 2.2 K. The sample is field cooled ($\mu_0 H$ ~ −0.01 T) through the Curie temperature (T_{Curie} ~ 20 K) to ensure a single magnetic domain with downward magnetization, as shown by the uniform MFM domain (Fig. 3A). The superconducting state is confirmed by the zero resistance from electrical transport measurements (fig. S6). By sweeping $\mu_0 H$ upward from −0.01 T, speckles of reversed magnetic domains (blue regions in Fig. 3B) randomly nucleate at $\mu_0 H$ = 0.047 T. As $\mu_0 H$ is increased further, the blue regions (i.e., the upward magnetic domains) expand at the expense of the red regions (i.e., the downward magnetic domains), gradually filling up the entire scan area (Fig. 3, C to G). At $\mu_0 H$ = 0.09 T, the MFM image is uniformly blue, corresponding to a uniform upward magnetization (Fig. 3H). The evolution of domain nucleation and domain wall propagation in the zero-resistance state demonstrates the coexistence of long-range ferromagnetic order and the emergent superconducting state (*34*).

The direct observation of magnetic domains also allows us to construct the ferromagnetic hysteresis loop. Figure 3I shows the $\mu_0 H$ dependence of the normalized magnetization M/M_s (where M_s is the saturated magnetization) at T =2.2 K, which is estimated from each MFM image using a differential image method (figs. S7 and S8) (*34*). The upward and downward domains are equally populated when M/M_s ~ 0 at coercive field $\mu_0 H_c$ ~ 0.061 T. This field value is in good agreement with the peak position of the root mean square value δf of the MFM signal (Fig. 3I) and the value obtained from the RMCD measurement at T = 2 K (Fig. 3J). In addition, similar magnetic domain behaviors are observed in the normal state at $T > T_{c,onset}$ ~ 12.4 K (fig. S9), demonstrating that the ferromagnetic order is not affected by the emergence of the superconducting state.

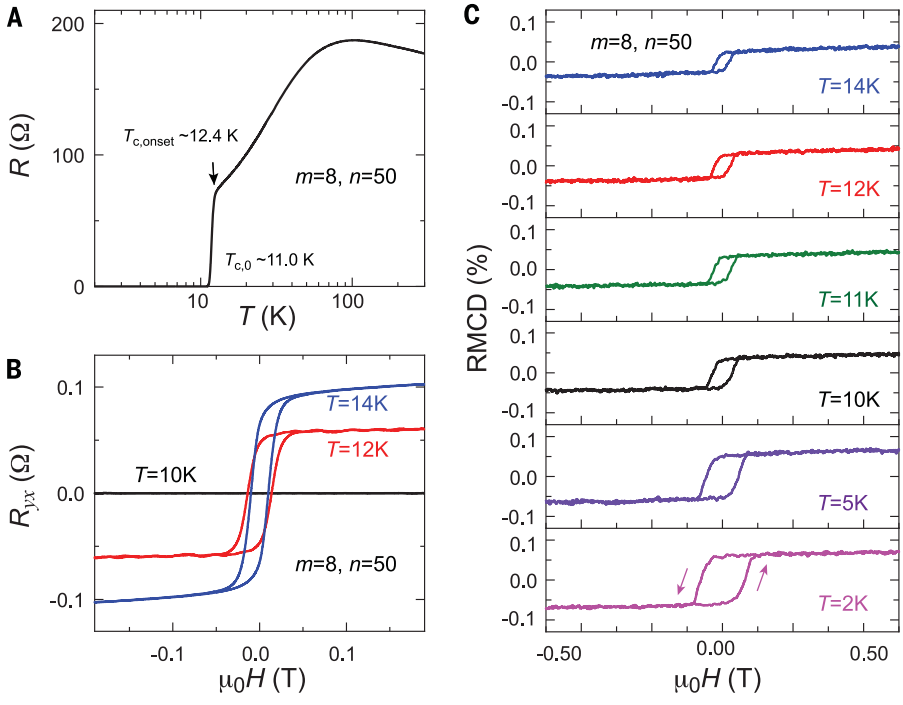

Fig. 2. Coexistence of ferromagnetism and superconductivity in Cr-doped $(Bi,Sb)_2Te_3$/FeTe heterostructures. All data are for the (8,50) heterostructure. (**A**) Temperature dependence of the sheet longitudinal resistance R. (**B**) Magnetic field $\mu_0 H$ dependence of the Hall resistance R_{yx} at T = 10 K (black), T = 12 K (red), and T = 14 K (blue). (**C**) $\mu_0 H$ dependence of the RMCD signal. Even for $T < T_{c,0}$, the sample shows a hysteresis loop, indicating the coexistence of ferromagnetism and superconductivity in the entire temperature range.

Proximity-induced superconductivity on the top surface of magnetic TI

To confirm and pinpoint the interface-induced superconductivity and the proximity effect in the ferromagnetic Cr-doped $(Bi,Sb)_2Te_3$ layer, we performed low-temperature STM/S measurements on (m,38) heterostructures of different m (Fig. 4 and figs. S10 to S15). For the 38UC FeTe layer that is partially covered by 1QL Cr-doped $(Bi,Sb)_2Te_3$ (i.e., the m < 1 sample; fig. S10A), the dI/dV spectra across the interface between 1QL Cr-doped $(Bi,Sb)_2Te_3$ and 38UC FeTe layers show the presence of the superconducting gap on the surface of 1QL Cr-doped $(Bi,Sb)_2Te_3$ but its absence on the FeTe surface at T = 310 mK (fig. S10B). This is consistent with our transport data (Fig. 1D and fig. S5). We note that the superconducting gap is spatially uniform and homogeneous on the surface of the m = 1 sample. This observation directly confirms the emergence of the interface-induced superconductivity in Cr-doped $(Bi,Sb)_2Te_3$/FeTe heterostructures.

Next, we focused on probing the proximity-induced superconducting gap on the top surface of the ferromagnetic Cr-doped $(Bi,Sb)_2Te_3$ layer with different thicknesses. Figure 4A shows the large-scale STM image of the (8,38) heterostructure. The surface of the Cr-doped $(Bi,Sb)_2Te_3$ layer exhibits spiral structures, which are characterized by atomically flat terraces with a width of a few tens of nanometers (*19*, *35*). The height of the terrace is ~1 nm, corresponding to the thickness of 1QL TI. The STM topographic image with atomic resolution (Fig. 4B) shows randomly distributed triangle-shaped dark features on the surface, which are Cr substitutions at Bi/Sb sites in the Cr-doped $(Bi,Sb)_2Te_3$ layer (*19*). Figure 4C shows the dI/dV spectra measured on the (m,38) heterostructures with different m at T = 310 mK. The suppressed spectral weight around the Fermi level signifies a superconducting gap on the top surface of the Cr-doped $(Bi,Sb)_2Te_3$ layer with m up to 10, suggesting a strong proximity effect. The gap feature can be fitted with the Dynes formula (fig. S11) (*36*). The resultant gap size is in good agreement with that of undoped TI/FeTe heterostructures in prior studies (*37*). With increasing m, the size of the superconducting gap gradually decreases (Fig. 4, C and D). This behavior resembles that found in undoped TI/FeTe heterostructures (*37*). Moreover, the superconducting gap shrinks with

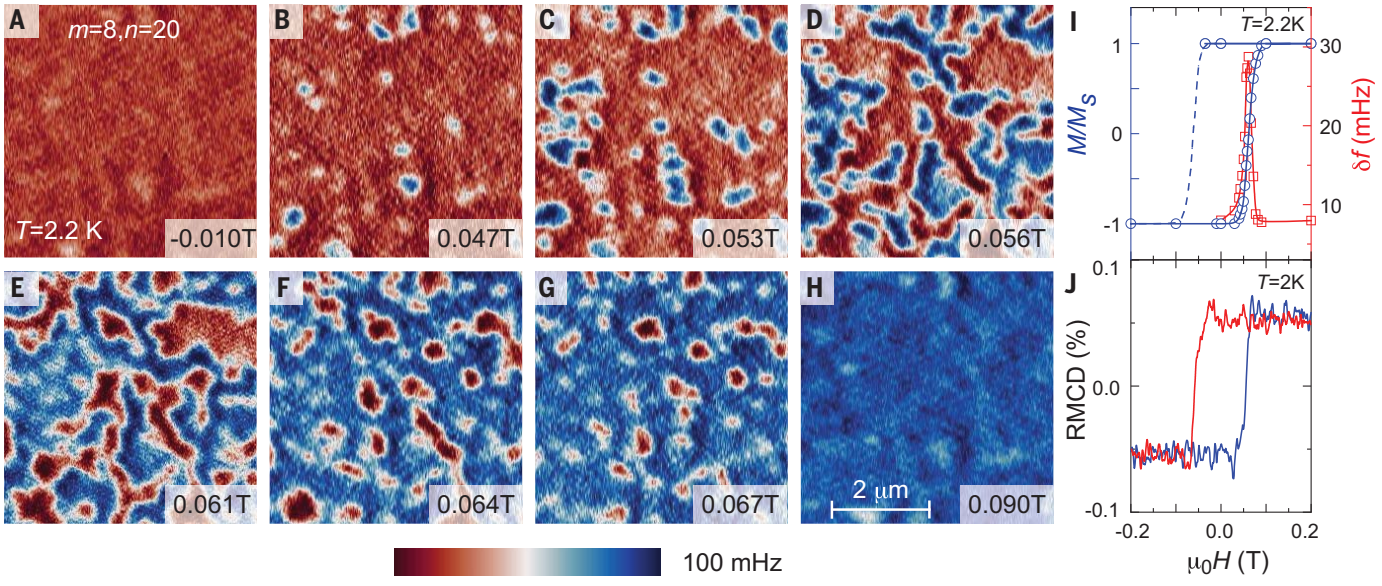

Fig. 3. Magnetization reversal process in the superconducting state of the Cr-doped $(Bi,Sb)_2Te_3$/FeTe heterostructures. (**A** to **H**) MFM images of magnetic domains in the (8,20) heterostructure measured at μ_0H = −0.01 T (A), 0.047 T (B), 0.053 T (C), 0.056 T (D), 0.061 T (E), 0.064 T (F), 0.064 T (G), and 0.090 T (H), respectively. All measurements are carried out at T = 2.2 K. (**I**) μ_0H dependence of the normalized magnetization M/M_s (blue) and the magnetic domain contrast δf (red). M/M_s is inferred from each MFM image using a differential image method. M_s is the saturated magnetization. δf is the root mean square value of each MFM image. (**J**) μ_0H dependence of the RMCD signal of the same heterostructure measured at T = 2 K.

increasing temperature and disappears at T ~ 6.5 K for m = 8 (Fig. 4E and fig. S12), slightly lower than the superconducting transition temperature found in transport measurements. This further confirms that the gap observed here is the proximity-induced superconducting gap on the top surface of the Cr-doped $(Bi,Sb)_2Te_3$ layer. Combining transport, RMCD, MFM, and STM/S results (Figs. 2 to 4), we thus unambiguously demonstrate the coexistence of superconductivity and ferromagnetism in the Cr-doped $(Bi,Sb)_2Te_3$ layer, consistent with an unconventional mechanism of superconductivity. Furthermore, our LE-μSR results suggest that the superconductivity does not suppress the magnetic order but instead occurs commensurately with a phase transition to a more uniform, ordered magnetic state centered at the Cr-doped $(Bi,Sb)_2Te_3$/FeTe interface (figs. S19 to S21).

To investigate the physical mechanism responsible for the coexistence of superconductivity and ferromagnetism and the superconducting pair-breaking mechanism, we varied the angle θ between the normal direction of the film and the direction of μ_0H and measured the values of the upper critical magnetic field μ_0H_{c2} at T = 1.5 K (fig. S16). We find μ_0H_{c2} to be independent of θ, thus confirming the superconductivity to be isotropic. We note that the large and isotropic μ_0H_{c2} ~ 44.5 T at T = 1.5 K exceeds the Pauli paramagnetic limit of μ_0H_p = $1.84T_c$ ~ 23.0 T for a conventional s-wave superconductor. This large μ_0H_{c2} may be responsible for the coexistence of ferromagnetism and superconductivity in Cr-doped $(Bi,Sb)_2Te_3$/FeTe heterostructures given that the pair-breaking mechanism from exchange coupling of ferromagnetism is similar to the Pauli paramagnetic effect (*38*). Moreover, the μ_0H_{c2} ~ T/T_c phase diagrams near T_c are fitted well with the Ginzburg-Landau (GL) theory in the 2D limit (figs. S17 and S18). The extracted in-plane GL coherence length is ~2.2 nm and the effective thickness of the superconducting region is ~10.4 nm for the (8,38) heterostructure (fig. S17). The latter value is less than the thickness of the FeTe layer (~24.7 nm), further implying that the superconductivity realized in Cr-doped $(Bi,Sb)_2Te_3$/FeTe heterostructures stems from an interfacial effect. Similar values of coherence length and effective superconducting thickness are also found in the (4,20) heterostructure (fig. S18) with the minimum thickness of the FeTe layer to achieve the zero-resistance state of superconductivity (Fig. 1E), corroborating the interfacial effect.

Discussion and outlook

The observed anisotropic μ_0H_{c2} near T_c but isotropic μ_0H_{c2} at low temperatures resembles that of iron chalcogenide crystals and thin films (*39*–*41*), suggesting that the superconductivity in our heterostructures originates from the FeTe layer when it is proximally coupled to the ferromagnetic Cr-doped $(Bi,Sb)_2Te_3$ layer. Therefore, the finite resistance in the $n \leq 16$ samples for $T < T_{c,onset}$ is likely a result of spatial confinement–induced phase fluctuations in the FeTe layer, which are induced by its low and inhomogeneous superfluid density (*42*, *43*). Although the parent phase of FeTe is an antiferromagnetic metal, superconductivity can emerge after its antiferromagnetic order is weakened by either elemental doping (*26*, *27*) or tensile stress (*28*). The hole-type charge carrier transfer effect across the Cr-doped $(Bi,Sb)_2Te_3$/FeTe interface might suppress the AFM order, triggering the formation of this interface-induced superconductivity (*44*). This possibility has been suggested by the observation of superconductivity in FeTe films with oxygen adsorption (*45*, *46*). The strain effect and RKKY interactions from the spin-momentum locked topological surface states (*47*) coupled with the interfacial FeTe layer may destabilize the antiferromagnetic order in the FeTe layer and thus promote superconductivity (*28*). A more complete understanding of the pairing mechanism requires further studies.

The most notable feature in our experiment is the long superconductivity proximity length in ferromagnetic Cr-doped $(Bi,Sb)_2Te_3$ layers up to m ~ 10 (Fig. 4D). The charge transfer occurring across the Cr-doped $(Bi,Sb)_2Te_3$/FeTe interface induces an asymmetric potential that leads to band bending, thus breaking inversion symmetry in the Cr-doped $(Bi,Sb)_2Te_3$ layer (fig. S22A). Our theoretical calculations show that this asymmetric potential plays a dual role in stabilizing the superconducting proximity effect in the Cr-doped $(Bi,Sb)_2Te_3$ layer. First, the asymmetric potential pushes the top surface state so that its energy is closer to the bulk conduction band bottom. This promotes

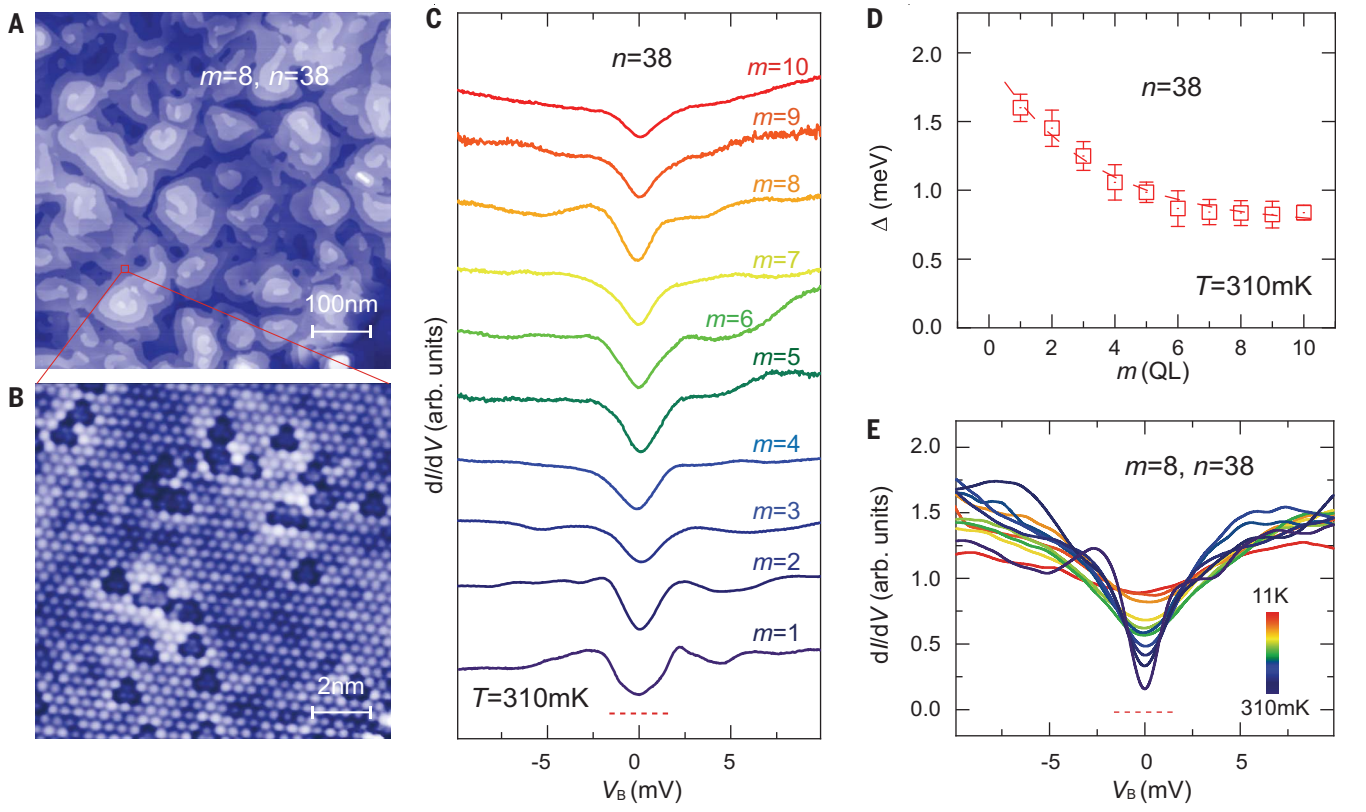

Fig. 4. STM/S characterization of *m*QL Cr-doped $(Bi,Sb)_2Te_3$/38 UC FeTe heterostructures. (**A**) Large-scale STM image of the (8,38) heterostructure showing spiral structures (sample bias V_B = +1.5 V, tunneling current I_t = 50 pA, T = 4.2 K). (**B**) Atomic-resolution STM image of the (8,38) heterostructure (V_B = −0.3 V, I_t = 500 pA, T = 4.2 K). The triangle-shaped dark features are from the Cr atoms embedded in the $(Bi,Sb)_2Te_3$ matrix. (**C**) m dependence of the dI/dV spectra on the surface of the (m,38) heterostructure (setpoint: V_B = +10 mV, I_t = 300 pA, T = 310 mK). (**D**) m dependence of the superconducting gap Δ on the surface of the (m,38) heterostructure. The values of the superconducting gap Δ are determined by fitting the dI/dV spectra. The error bars are the results of the fitting process and spatial distribution. The dashed line is a guide to the eye. (**E**) Temperature dependence of the dI/dV spectra on the surface of the (8, 38) heterostructure (setpoint: V_B = +10 mV, I_t = 300 pA). The red dashed lines in (C) and (E) correspond to the zero dI/dV values of the (1,38) and (8,38) heterostructures, respectively. The color bar in (E) is on a linear scale.

a strong hybridization between the top surface state and the bulk conduction bands, resulting in a very long penetration depth of the top surface state across the entire Cr-doped $(Bi,Sb)_2Te_3$ layer (fig. S22). Therefore, there is a strong superconductor proximity effect of the top surface state from the superconductivity at the Cr-doped $(Bi,Sb)_2Te_3$/FeTe interface. Next, the asymmetric potential breaks the inversion symmetry, leading to the emergence of a mixed pairing state with both singlet and triplet components (*20*). This inversion symmetry breaking removes the energy degeneracy between the top and bottom surface states. Owing to the spin-momentum locking of topological surface states, electron spin at the Fermi surfaces becomes predominantly pinned into the 2D plane, while the z-directional magnetization only induces a minor tilt in the electron spin (fig. S23, A and B). Consequently, the thickness dependence of the proximity-induced superconducting gap exhibits a monotonic decay with a long proximity length (fig. S23C), in good agreement with our experimental observations (Fig. 4D). Therefore, we demonstrate the existence of long-range superconducting proximity in magnetic TI, even with a spin-singlet superconductivity at the magnetic TI/FeTe interface. Given the coexistence of ferromagnetism and superconductivity, our theoretical analysis of the topological phase diagram (fig. S24) also establishes the MBE-grown Cr-doped $(Bi,Sb)_2Te_3$/FeTe heterostructure with an atomically sharp interface as a natural platform to search for the chiral TSC phase (*14*).

REFERENCES AND NOTES

1. J. Bardeen, L. N. Cooper, J. R. Schrieffer, *Phys. Rev.* **106**, 162–164 (1957).
2. J. Bardeen, L. N. Cooper, J. R. Schrieffer, *Phys. Rev.* **108**, 1175–1204 (1957).
3. A. Ohtomo, H. Y. Hwang, *Nature* **427**, 423–426 (2004).
4. N. Reyren *et al.*, *Science* **317**, 1196–1199 (2007).
5. A. Gozar *et al.*, *Nature* **455**, 782–785 (2008).
6. J. Alicea, *Phys. Rev. B* **81**, 125318 (2010).
7. R. M. Lutchyn, J. D. Sau, S. Das Sarma, *Phys. Rev. Lett.* **105**, 077001 (2010).
8. Y. Oreg, G. Refael, F. von Oppen, *Phys. Rev. Lett.* **105**, 177002 (2010).
9. V. Mourik *et al.*, *Science* **336**, 1003–1007 (2012).
10. A. Y. Kitaev, *Ann. Phys.* **303**, 2–30 (2003).
11. X. L. Qi, S. C. Zhang, *Rev. Mod. Phys.* **83**, 1057–1110 (2011).
12. M. Z. Hasan, C. L. Kane, *Rev. Mod. Phys.* **82**, 3045–3067 (2010).
13. L. Fu, C. L. Kane, *Phys. Rev. Lett.* **100**, 096407 (2008).
14. X. L. Qi, T. L. Hughes, S. C. Zhang, *Phys. Rev. B* **82**, 184516 (2010).
15. J. Wang, Q. Zhou, B. Lian, S. C. Zhang, *Phys. Rev. B* **92**, 064520 (2015).
16. M. Kayyalha *et al.*, *Science* **367**, 64–67 (2020).
17. L. Fu, C. L. Kane, *Phys. Rev. Lett.* **102**, 216403 (2009).
18. A. R. Akhmerov, J. Nilsson, C. W. J. Beenakker, *Phys. Rev. Lett.* **102**, 216404 (2009).
19. C.-Z. Chang, C.-X. Liu, A. H. MacDonald, *Rev. Mod. Phys.* **95**, 011002 (2023).
20. A. I. Buzdin, *Rev. Mod. Phys.* **77**, 935–976 (2005).
21. Q. L. He *et al.*, *Nat. Commun.* **5**, 4247 (2014).
22. J. Liang *et al.*, *Proc. Natl. Acad. Sci. U.S.A.* **117**, 221–227 (2020).
23. H. J. Zhang *et al.*, *Nat. Phys.* **5**, 438–442 (2009).
24. Y. L. Chen *et al.*, *Science* **325**, 178–181 (2009).
25. D. Hsieh *et al.*, *Phys. Rev. Lett.* **103**, 146401 (2009).
26. Y. Mizuguchi, F. Tomioka, S. Tsuda, T. Yamaguchi, Y. Takano, *Appl. Phys. Lett.* **94**, 012503 (2009).
27. F. S. Li *et al.*, *Phys. Rev. B* **91**, 220503 (2015).
28. Y. Han *et al.*, *Phys. Rev. Lett.* **104**, 017003 (2010).
29. See supplementary materials.
30. X. Yao *et al.*, *Nano Lett.* **21**, 6518–6524 (2021).
31. C. Z. Chang *et al.*, *Science* **340**, 167–170 (2013).
32. V. J. Emery, S. A. Kivelson, *Nature* **374**, 434–437 (1995).
33. C. Yang *et al.*, *Nature* **601**, 205–210 (2022).
34. W. B. Wang *et al.*, *Nat. Phys.* **14**, 791–795 (2018).
35. Y. Liu, M. Weinert, L. Li, *Phys. Rev. Lett.* **108**, 115501 (2012).
36. R. C. Dynes, V. Narayanamurti, J. P. Garno, *Phys. Rev. Lett.* **41**, 1509–1512 (1978).
37. H. Qin *et al.*, *Nano Lett.* **20**, 3160–3168 (2020).
38. F. S. Bergeret, A. F. Volkov, K. B. Efetov, *Rev. Mod. Phys.* **77**, 1321–1373 (2005).
39. M. G. Fang *et al.*, *Phys. Rev. B* **81**, 020509 (2010).
40. S. Khim *et al.*, *Phys. Rev. B* **81**, 184511 (2010).

41. P. Mele, *Sci. Technol. Adv. Mater.* **13**, 054301 (2012).
42. D. Chatzopoulos *et al*., *Nat. Commun.* **12**, 298 (2021).
43. D. Cho, K. M. Bastiaans, D. Chatzopoulos, G. D. Gu, M. P. Allan, *Nature* **571**, 541–545 (2019).
44. K. Owada *et al*., *Phys. Rev. B* **100**, 064518 (2019).
45. W. D. Si *et al*., *Phys. Rev. B* **81**, 092506 (2010).
46. W. Ren *et al*., *Materials* **14**, 4584 (2021).
47. Q. Liu, C. X. Liu, C. Xu, X. L. Qi, S. C. Zhang, *Phys. Rev. Lett.* **102**, 156603 (2009).
48. C.-Z. Chang, Data for "Interface-Induced Superconductivity in Magnetic Topological Insulators," Harvard Dataverse, version 2 (2023); https://doi.org/10.7910/DVN/MH1UYX.

ACKNOWLEDGMENTS

We thank Y. Cui, L. Fu, L. Hu, F. Li, B. Xia, D. Xiao, H. Zhang, and H. Zheng for helpful discussions; H. Wang for STEM sample preparations; and S. H. Lee for high magnetic field sample preparations. **Funding:** This work was primarily supported by US Department of Energy (DOE) grant DE-SC0023113, including the MBE growth, ARPES, and electrical transport measurements. The sample characterization was partially supported by an NSF-CAREER award (DMR-1847811) and the Penn State MRSEC for Nanoscale Science (DMR-2011839). The MBE growth and the ARPES measurements were partially performed in the NSF-supported 2DCC MIP facility (DMR-2039351). The STM/S measurements were partially supported by an Army Research Office grant (W911NF2210159). The theoretical calculations were partially supported by an NSF grant (DMR-2241327) and Penn State MRSEC for Nanoscale Science (DMR-2011839). The MFM measurements were supported by DOE grant DE-SC0018153. The RMCD measurements were supported by an Air Force Office of Scientific Research grant (FA9550-21-1-0177). Work done at the National High Magnetic Field Laboratory was supported by the NSF (DMR-1644779 and DMR-2128556) and the State of Florida. C.-Z.C. acknowledges support from the Gordon and Betty Moore Foundation's EPiQS Initiative (grant GBMF9063 to C.-Z.C.). Certain commercial equipment, instruments, software, or materials are identified in this paper to specify the experimental procedure adequately. Such identifications are not intended to imply recommendation or endorsement by the National Institute of Standards and Technology, nor are they intended to imply that the materials or equipment identified are necessarily the best available for the purpose. **Author contributions:** C.-Z.C. conceived of and designed the experiment. H.Y. performed the MBE growth, ARPES, and PPMS transport measurements. Y.-F.Z., Z.W., and S.P. performed the STM/S measurements. Y.-T.C. and W.W. performed the MFM measurement. J.C. and X.X. performed the RMCD measurements. J.S., L.E.W., and H.Y. performed the high magnetic field transport measurements. K.W. carried out the TEM measurements. T.P., Z.S., A.S., P.P.B., and A.J.G. performed LE-μSR measurements. X.W., R.M., and C.-X.L. provided theoretical support. H.Y., Y.-T.C., X.W., W.W., C.-X.L., and C.-Z.C. analyzed the data and wrote the manuscript with input from all authors. **Competing interests:** The authors declare that they have no competing interests. **Data and materials availability:** All data in the main text and the supplementary materials, as well as code for theoretical calculations, are available in Harvard Dataverse (*48*).

SUPPLEMENTARY MATERIALS

science.org/doi/10.1126/science.adk1270
Materials and Methods
Supplementary Text
Figs. S1 to S24
References (*49*–*63*)

Submitted 29 July 2022; resubmitted 3 August 2023
Accepted 10 January 2024
10.1126/science.adk1270